IAC-12.C1.7.2

REPRESENTATIONS OF HIGHER-DIMENSIONAL POINCARÉ MAPS WITH APPLICATIONS TO SPACECRAFT TRAJECTORY DESIGN

Amanda F. Haapala*
Purdue University, United States of America
ahaapala@purdue.edu

Kathleen C. Howell†
Purdue University, United States of America
howell@purdue.edu

The Circular Restricted Three-Body Problem (CR3BP) serves as a useful framework for preliminary trajectory design in a multi-body force environment. While the CR3BP offers a simplified model with useful symmetries, trajectory design in this dynamical regime is often nontrivial. It is essential to gain insight into the available solution space to generate trajectories that meet a variety of constraints. The Poincaré map is a powerful tool that, in combination with a constraint on the energy level, allows a reduction in dimension such that, for the planar problem, the system is reduced to two-dimensions and the phase space is fully represented by the projection onto a plane. In the spatial problem, however, Poincaré maps must represent at least four states and are therefore challenging to visualize. In this investigation, a method to represent the information in higher-dimensional Poincaré maps using a planar visualization is explored and is applied to trajectory design. Four-dimensional map representations are demonstrated to compute transfers, including heteroclinic and homoclinic connections, between periodic and quasi-periodic orbits in the spatial problem. Alternative maps, such as the periapse Poincaré map, require that the full six Cartesian states be represented. Sample six-dimensional periapse map representations are generated and are employed to locate families of periodic orbits about the Moon, as well as transfers to these orbits via transit trajectories.

Introduction

The Circular Restricted Three-Body Problem (CR3BP) serves as a useful framework for preliminary trajectory design in a multi-body force environment. Libration point orbits are well known solutions[3,4,8,10,11,15,30] that have been employed in numerous missions. Missions to libration point orbits in the Sun-Earth system include observatories in the vicinity of L_1 (ISEE-3,[21] SOHO,[23] ACE,[22] WIND,[22] Genesis[22]), and near L_2 (WMAP[24] and the Herschel and Planck Space Observatories[9]). ARTEMIS was the first libration point mission in the Earth-Moon system; two spacecraft were maintained in large quasi-periodic orbits about the L_1 and L_2 points before entering long-term lunar orbits. While the existence of periodic and quasi-periodic solutions near the libration points in the CR3BP is generally well understood, the design of trajectories that incorporate these orbits is nontrivial. To generate trajectories that meet a variety of constraints, tools that offer insight into the available solution space are essential. The Poincaré map is a powerful tool that is useful to evaluate available solutions and to compute trajectories with specified characteristics. In combination with a constraint on energy level, Poincaré maps allow a reduction in dimension such that, for the planar problem, the system is reduced to two dimensions and the state space is fully represented via a planar projection. In the spatial problem, Poincaré maps must represent at least four state variables. In this investigation, a method to represent the available information in higher-dimensional Poincaré maps is explored and is applied to trajectory design.

A variety of different approaches to represent higher-dimensional maps is useful to be more effective in trajectory design. To examine behavior in the vicinity of the collinear libration points, Jorba and Masdemont (1999),[17] as well as Gómez et al. (2005),[13] obtain higher-order normal form expansions of the Hamiltonian in the vicinity of the equilibrium points to decouple the stable and unstable motion. Removing unstable behavior via a reduction to the center manifold yields a system with two degrees of freedom; thus, maps associated with periodic and quasi-periodic orbits in the spatial problem for a particular energy level are two-dimensional. Gómez et al. (2004)[12] compute the stable/unstable manifolds asymptotic to the center manifold associated with the collinear points for a particular energy level and employ a Poincaré map to reduce the dimension of the problem. By selecting two additional parameters, the four-dimensional maps

*Ph.D. Student, School of Aeronautics and Astronautics
†Hsu Lo Professor, School of Aeronautics and Astronautics

are reduced to two-dimensions and a planar visualization of the map is achieved, thus, the problem of locating trajectories with prescribed characteristics is more tractable. Paskowitz and Scheeres (2006)[25] employ periapse maps to classify trajectory behavior in the spatial problem; these authors represent higher-dimensional maps by plotting vectors such that the basepoint represents the three-dimensional position state and the magnitude and direction of the vector indicate the velocity at periapsis, as well as by plotting inclination as a function of periapse radius. A variety of reprentations for multivariate data sets to enable visual inspection of the data are discussed by Ward (2002).[32] In this investigation, planar map representations, employed to visualize four or more state variables, are demonstrated and employed in various mission design scenarios. These higher-dimensional Poincaré map representations are used to search for maneuver-free transfers between libration point orbits in the spatial problem in both the Earth-Moon and Sun-Earth systems. Poincaré maps are also useful to locate solutions such as transit and non-transit trajectories[5,12,19] by propagating a batch of initial conditions and examining subsequent returns to the map. The periapse Poincaré map has been employed by several researchers[25,31] to investigate available trajectories in both the planar and spatial problems. To fully represent the periapse map in terms of Cartesian coordinates in the spatial problem, all six states must be represented. Sample six-dimensional periapse map representations are generated and regions of transit, as well as regions of long-term capture, emerge. Periodic orbits about the Moon are located by visual inspection of the structures associated with nearby capture orbits on the map, and are used to initialize families of periodic orbits. By observing map crossings associated with transit trajectories in the vicinity of the periodic orbits, a sample transfer from the Earth to one of these lunar capture orbits is computed.

Fundamental Motions in the CR3BP

In the CR3BP, the motion of a spacecraft, assumed massless, is examined as it moves in the vicinity of two primary bodies, P_1 and P_2. A rotating frame, centered at the system barycenter, B, is defined such that the rotating $\hat{x}$-axis is directed from the larger primary (P_1) to the smaller (P_2), the $\hat{z}$-axis is parallel to the direction of the angular velocity of the primary system, and the $\hat{y}$-axis completes the dextral orthonormal triad. The system is non-dimensionalized using the following characteristic quantities: total mass, $m^* = m_1 + m_2$; the distance between the primaries, ℓ^*; and, characteristic time, $t^* = \sqrt{\frac{\ell^{*3}}{Gm^*}}$. The non-dimensional distances to the primaries are $r_1 = \mu$, $r_2 = 1-\mu$, where $\mu = \frac{m_2}{m^*}$. The position vectors, defined in terms of rotating coordinates relative to B, P_1, and P_2, are $\bar{r} = x\hat{x} + y\hat{y} + z\hat{z}$, $\bar{r}_{13} = (x-\mu)\hat{x} + y\hat{y} + z\hat{z}$, and $\bar{r}_{23} = (x-1+\mu)\hat{x} + y\hat{y} + z\hat{z}$. The first-order vector equation of motion for the CR3BP is written with respect to the rotating frame in non-dimensional variables as $\dot{\bar{x}} = \bar{f}(\bar{x})$, where $\bar{f} = \left[\begin{array}{ccccccc} \dot{x}, & \dot{y}, & \dot{z}, & 2\dot{y}+\Omega_x, & -2\dot{x}+\Omega_y, & \Omega_z \end{array}\right]^T$. The pseudo-potential, Ω, is defined $\Omega(x,y,z) = \frac{1-\mu}{r_{13}} + \frac{\mu}{r_{23}} + \frac{1}{2}(x^2+y^2)$, and the quantities Ω_x, Ω_y, Ω_z represent partial derivatives of Ω with respect to rotating variables. Five libration points exist, and are depicted in Fig. 1. The integral of the motion, denoted the Jacobi constant, is represented as $C = 2\Omega(x,y,z) - v^2$, where $v = \sqrt{\dot{x}^2 + \dot{y}^2 + \dot{z}^2}$.

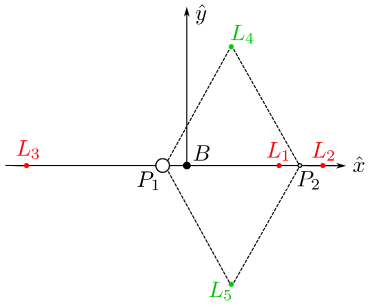

Fig. 1 Equilibrium points in the CR3BP

Within the framework of the CR3BP, several fundamental solutions exist that prove useful in mission design. Several families of periodic and quasi-periodic solutions exist within the vicinity of the collinear libration points and have been studied by several researchers.[3,4,8,10,11,15,18,30] Some examples include the planar and vertical Lyapunov orbits, as well as the family of halo orbits; sample orbits about the L_1 and L_2 points in the Earth-Moon system are plotted in Fig. 2.

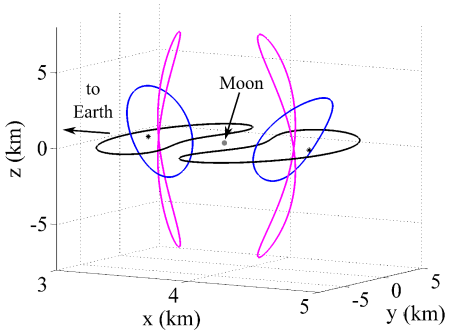

Fig. 2 Sample Lyapunov (black), halo (blue), and vertical orbits (magenta) for $C = 3.05$ in the Earth-Moon system

For unstable periodic orbits in the CR3BP, invariant manifold structures exist that provide transport into and away from the orbits. The stable/unstable manifolds are computed by introducing a perturbation in the state along a periodic orbit (period T) in the direction of the stable/unstable eigenvector. Assume that

$\lambda^S < 1$ and $\lambda^U = 1/\lambda_s$ are the stable and unstable eigenvalues from the monodromy matrix, $\Phi(t_0+T, t_0)$, corresponding to an unstable periodic orbit. Let $\bar{w}^S$ and $\bar{w}^U$ be their associated eigenvectors, computed by solving the equations, $\Phi(t_0+T, t_0)\bar{w}^S = \lambda^S \bar{w}^S$, $\Phi(t_0+T, t_0)\bar{w}^U = \lambda^U \bar{w}^U$. Define $\bar{w}^+$, $\bar{w}^-$ as the two directions associated with each eigenvector. The local half-manifolds, W^{U-}_{loc} and W^{S-}_{loc}, are approximated by introducing a perturbation relative to the fixed point, $\bar{x}^*$, along the periodic orbit in the directions $\bar{w}^{U-}$ and $\bar{w}^{S-}$, respectively. Likewise, a perturbation relative to $\bar{x}^*$ in the directions $\bar{w}^{U+}$ and $\bar{w}^{S+}$, respectively, produces the local half-manifolds W^{U+}_{loc} and W^{S+}_{loc}. The step along the direction of the eigenvector is denoted d, and the initial states along the local stable manifolds are $\bar{x}^{S+} = \bar{x}^* + d \cdot \bar{w}^{S+}$, $\bar{x}^{S-} = \bar{x}^* - d \cdot \bar{w}^{S-}$, where $\bar{w}^{S+}$ and $\bar{w}^{S-}$ are normalized so that the vector containing the position components of the eigenvector is of unit length; this normalization provides a physical meaning for the value of d as a distance. The value of d is critical because it determines the accuracy with which the local manifolds are approximated. For the purposes of this investigation, d is selected so that propagating the states $\bar{x}^{S+}$, $\bar{x}^{S-}$ over the interval $[0, 2T]$ in forward-time yields a trajectory that remains in the vicinity of the periodic orbit. The local stable manifolds are globalized by propagating the states $\bar{x}^{S+}$ and $\bar{x}^{S-}$ in reverse time in the nonlinear model. This process yields the numerical approximation for the global manifolds $W^{S+}_{\bar{x}^*}$ and $W^{S-}_{\bar{x}^*}$, respectively. The same procedure is employed to approximate the global unstable manifolds, $W^{U+}_{\bar{x}^*}$ and $W^{U-}_{\bar{x}^*}$. The collection of all stable and unstable manifolds forms a surface that reflects asymptotic flow into and away from the periodic orbit.

Poincaré Maps

The Poincaré map is a valuable tool to gain insight into the complicated dynamics in the CR3BP. Defining a surface of section, Σ, a map is generated by propagating initial conditions and displaying intersections of the resulting trajectories with Σ. The use of a Poincaré section, in addition to a constraint on the value of Jacobi constant, reduces the dimension of the system by two. In the planar problem, the state space is, therefore, entirely represented by the projection onto a plane. As an example, consider the Poincaré map appearing in Fig. 3 that depicts a projection of the intersections of the stable manifold of a planar L_1 Lyapunov orbit and the unstable manifold of an L_2 Lyapunov with the surface Σ defined by $x = 1 - \mu$ for $C = 3.15$ in the Earth-Moon system; these intersections with Σ form contours in the $y - \dot{y}$ phase space. The map is one-sided, that is, only crossings in one direction ($\dot{x} > 0$ in this example) are considered. For each point on the map, $x = 1 - \mu$, y and $\dot{y}$ are plotted in the map, and $\dot{x}$ is computed from the specified value of Jacobi constant. Thus, an

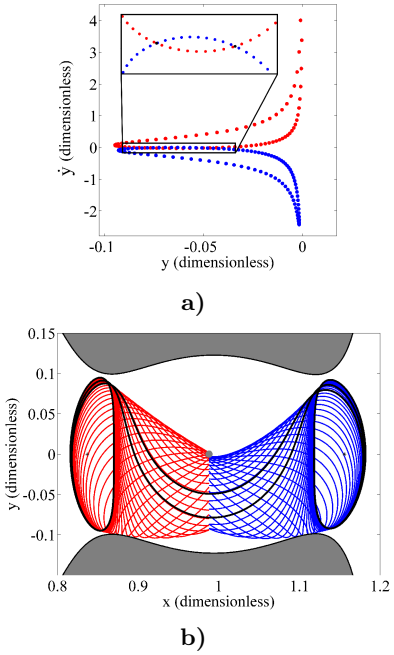

Fig. 3 A Poincaré map is demonstrated for the planar problem; two heteroclinic connections are determined from the intersection of the contours on the map

intersection of the two contours in the $y - \dot{y}$ plane indicates a match in the full state space, and the existence of a heteroclinic connection between the L_1 and L_2 Lyapunov orbits. The contours in Fig. 3(a) intersect in two locations, indicated by black dots on the map, yielding two distinct heteroclinic transfers that are plotted in black in Fig. 3(b). While it is straightforward to locate heteroclinic connections in the planar CR3BP (PCR3BP), the computation of analagous solutions in the spatial CR3BP (SCR3BP) is non-trivial. In the spatial problem, the reductions obtained from constraining the value of Jacobi constant and employing a Poincaré map yield a four-dimensional state space. Thus, intersections with Σ are no longer fully represented by a planar projection. A number of researchers employ various approaches to represent the higher-dimensional Poincaré map.[12,13,17,25,32] In this investigation, a planar visualization is employed to display information for all states simultaneoulsy.

Maps in the SCR3BP must depict at least four state variables to fully represent intersections with Σ. Such a representation is supplied by a vector, which may be used to represent two states through the position of the basepoint of the vector and two states through the magnitude and direction of the vector. Thus, the points on the Poincaré maps from the planar problem (e.g., Fig. 3(a)) may be replaced with vectors in the spatial problem to represent four state variables while still employing a planar visualization; these vectors serve as glyphs,[32] i.e., graphical objects whose physical characteristics are determined by the data set, that enable visualization of the states associated with cross-

ings of the Poincaré map. As an example, for Σ defined by $x = 1 - \mu$ and a specified value of Jacobi constant, the state variables y, z, $\dot{y}$, $\dot{z}$ should be displayed on the map; such a visualization appears in Fig. 4(a). The basepoint of the vector represents the position (y, z), and provides the origin for a second coordinate frame that is employed to represent the velocity states $\dot{y}$ and $\dot{z}$. The remaining state, $\dot{x}$, is computed from the Jacobi constant. This representation may be modified for use with alternative types of maps, for example, the periapse map. Periapse maps are generated by considering intersections with the surface $\Sigma = \{\dot{\rho} = 0\}$, where ρ represents the magnitude of the position vector of the satellite, P_3, relative to either P_1 or P_2. The state is represented in spherical coordinates by five variables: the radius, ρ, in-plane angle θ, out-of-plane angle ϕ, and the angular rates $\dot{\theta}$, $\dot{\phi}$. One variable is eliminated through a constraint on the value of Jacobi constant, and the state is fully defined through four variables. Thus, a periapse map depicting $(\theta, \phi, \dot{\theta}, \dot{\phi})$ represents the full state associated with a periapsis for a specified value of C. A map displayed in spherical coordinates may not offer an intuitive representation for the state space, however. Alternatively, the glyphs

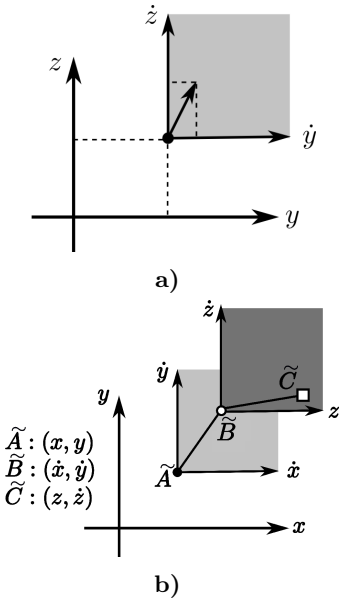

Fig. 4 Representations of higher-dimensional Poincaré maps

defined to represent four states are extended to represent the six Cartesian states, as depicted in Fig. 4(b). In this map, information from the six state space variables is displayed using a glyph comprised of a pair of connected vectors (subsequently denoted as a vector 'chain'). The base point corresponding to the first coordinate plane is defined in the $x - y$ plane. Then, the planar projection of the periapsis position appears as the black point $(\tilde{A})$ at location (x, y) in the $x - y$ plane. Point $\tilde{A}$ serves as the base point for the second coordinate frame, defined as the $\dot{x} - \dot{y}$ plane, and the circle $(\tilde{B})$ represents the planar velocity state $(\dot{x}, \dot{y})$. A third coordinate plane is defined, with the point $\tilde{B}$ as its origin, and represents the out-of-plane components $z - \dot{z}$. Thus, the square $(\tilde{C})$ reflects the coordinates $(z, \dot{z})$ and the full state is represented by the 'chain' $\tilde{A}-\tilde{B}-\tilde{C}$. Thus, a visualization for the full state space associated with crossings of the Poincaré map is realized in a two-dimensional image. The representations of multi-variate data points employed in this study are similar to the 'stick-figure' icons demonstrated by Pickett and Grinstein (1988).[27]

Heteroclinic and Homoclinic Connections between Periodic and Quasi-periodic Orbits

The Poincaré map is a useful tool in the location of maneuver-free heteroclinic and homoclinic connections between periodic or quasi-periodic orbits. Koon et al. (2000),[19] Gómez et al. (2005),[13] Barrabés et al. (2009),[1,2] and Parker et al. (2010)[26] demonstrate the use a variety of Poincaré maps to locate heteroclinic connections between planar orbits in the CR3BP; Gómez et al. (2004, 2005)[12,13] produce heteroclinic and homoclinic connections associated with Lissajous orbits.

Targeting Heteroclinic and Homoclinic Connections

Poincaré maps are useful in the location of an initial guess to initiate a search for a heteroclinic connection, however, a differential corrections process must be applied to enforce continuity along the transfer arc. Two differential corrections procedures are employed in this investigation to compute heteroclinic connections (note that the connections are heteroclinic in a numerical sense, that is, the trajectories are corrected to be continuous to within a tolerance of ∼1 cm and $\sim 1 \times 10^{-8}$ m/s in the Sun-Earth examples and ∼ 0.1 mm and $\sim 1 \times 10^{-9}$ m/s for Earth-Moon transfers) between a) periodic or b) quasi-periodic orbits, where the orbits exist in either the planar or spatial problems, and are described as follows:

Connecting Periodic Orbits

To locate heteroclinic transfers that depart from periodic orbit 1 and approach periodic orbit 2, consider the schematic in Fig. 5. Let the point numbered 1

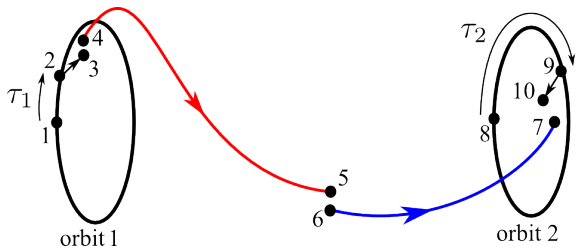

Fig. 5 Defining the variables employed in targeting algorithms for transfers between orbits

represent the initial state $\bar{x}_1(t_{10})$ along periodic orbit 1, where $T_1 = t_{1f} - t_{10}$ is the orbital period. Point 2 represents the location $\bar{x}_1(\tau_1)$ along the orbit after a coast time of τ_1; departure onto the unstable manifold occurs at this location by stepping along the unstable eigenvector direction $\bar{w}^{U+}$. Point 3 represents this step and is computed as $\bar{x}_{m1} = \bar{x}_1(\tau_1) + d_1 \cdot \bar{w}^{U+}$, where d_1 may be positive or negative. The initial state, $\bar{x}_u(t_{u0})$, along the unstable manifold arc is represented as point 4, and point 5 corresponds to the final state, $\bar{x}_u(t_{uf})$, after a propagation time of $t_{uf} - t_{u0}$. Similarly, points 6 and 7 depict the initial and final states, $\bar{x}_s(t_{s0})$ and $\bar{x}_s(t_{sf})$, along the stable manifold associated with orbit 2. The states associated with points 5 and 6 are selected from the map to generate the intial guess for the transfer. Orbit 2 is defined by the initial state $\bar{x}_2(t_{20})$ at point 8, and $T_2 = t_{2f} - t_{20}$ is the orbit period. Finally, point 9 represents the location $\bar{x}_2(\tau_2)$ along the orbit after a coast time of τ_2, at which point the step onto the stable manifold, $\bar{x}_{m2} = \bar{x}_2(\tau_2) + d_2 \cdot \bar{w}^{S+}$, is depicted by point 10; note that d_2 may be positive or negative. In the corrections process, the quantities contained in $\bar{X}$ are allowed to vary in order to satisfy the constraint $\bar{F} = \bar{0}$, where

$$\bar{X} = \begin{bmatrix} \bar{x}_1(t_{10}) \\ T_1 \\ \bar{x}_2(t_{20}) \\ T_2 \\ \tau_1 \\ \tau_2 \\ \bar{x}_u(t_{uf}) \\ T_u \\ \bar{x}_s(t_{s0}) \\ T_s \\ \beta_1 \\ \beta_2 \end{bmatrix}, \quad \bar{F} = \begin{bmatrix} x_1(t_{1f}) - x_1(t_{10}) \\ y_1(t_{1f}) - y_1(t_{10}) \\ z_1(t_{1f}) - z_1(t_{10}) \\ \dot{x}_1(t_{1f}) - \dot{x}_1(t_{10}) \\ \dot{y}_1(t_{1f}) - \text{sign}(\dot{y}_1(t_{10})) \cdot \beta_1^2 \\ \dot{z}_1(t_{1f}) - \dot{z}_1(t_{10}) \\ x_2(t_{2f}) - x_2(t_{20}) \\ y_2(t_{2f}) - y_2(t_{20}) \\ z_2(t_{2f}) - z_2(t_{20}) \\ \dot{x}_2(t_{2f}) - \dot{x}_2(t_{20}) \\ \dot{y}_2(t_{2f}) - \text{sign}(\dot{y}_2(t_{20})) \cdot \beta_2^2 \\ \dot{z}_2(t_{2f}) - \dot{z}_2(t_{20}) \\ \bar{x}_s(t_{s0}) - \bar{x}_u(t_{uf}) \\ \bar{x}_u(t_{u0}) - \bar{x}_{m1} \\ \bar{x}_s(t_{sf}) - \bar{x}_{m2} \end{bmatrix}$$

Solutions that satisfy the equation $\bar{F} = \bar{0}$ represent a fully continuous transfer arc between two periodic orbits, to within the specified tolerance. A discontinuity exists between the manifold state $\bar{x}_{mi}$ and orbit state $\bar{x}_i(\tau_i)$ ($i = 1$ or 2); however, the value of d_i is selected such that propagating $\bar{x}_{mi}$ for $2 \cdot T_i$ in reverse-time for $i = 1$ or forward-time for $i = 2$ yields a trajectory that remains in the vicinity of to the periodic orbit. Due to the sensitivity of these trajectories to perturbations in the initial conditions, additional patch points are included along the periodic orbits and the manifold arcs. Because the periodic orbits are not propagated as one continuous arc, the identity $\Phi(t_{1f}, t_{10}) = \Phi(t_{1f}, t_{1n})\Phi(t_{1n}, t_{1(n-1)}) \ldots \Phi(t_{11}, t_{10})$, where $t_{10} < t_{11} < \ldots < t_{1n} < t_{1f}$, is employed to approximate the monodromy matrix over one orbit during the differential corrections process. By selecting orbit 2 equal to orbit 1, homoclinic connections associated with periodic orbits are located.

Connecting Quasi-Periodic Orbits

In some cases, the targeting algorithm to locate a transfer between periodic orbits does not converge (i.e., a free transfer between periodic orbits does not exist in the vicinity of the initial guess). Then, the constraint that orbits 1 and 2 be periodic is relaxed and a connection between quasi-periodic orbits is sought. In this case, multiple revolutions around orbits 1 and 2 are incorporated into the initial guess, in addition to the unstable and stable manifold arcs from periodic orbits 1 and 2, respectively. Nodes are distributed along the orbits and manifold arcs, and the full state at each node is allowed to vary, in addition to the time-of-flight along each segment. Continuity is enforced between subsequent segments to yield a fully continuous transfer between quasi-periodic orbits in the vicinity of the original periodic orbits.

Heteroclinic Connections between L_1 and L_2 Halo Families

The halo orbit families in the CR3BP are composed of orbits that are symmetric across the $x - z$ plane, many of which have an unobscured line-of-sight to each of the primary locations. To demonstrate the use of the four-dimensional map representations to locate heteroclinic connections, consider, as an example, the search for free transfers between L_1 northern and L_2 southern halo orbits in the Sun-Earth system (low-thrust transfers between northern and southern halo orbits are demonstrated to be more fuel efficient than transfers between the northern families by Stuart et al. (2010)[29]). Halo orbits in the vicinity of L_1 and L_2 for the Jacobi value C = 3.00074 are computed and the unstable and stable manifolds, respectively, are computed and propagated until their first crossing of the plane defined by $\Sigma = \{x = 1 - \mu\}$. The manifolds, surface of section, and manifold crossings are plotted in Fig. 6(a). In the figure, red represents the unstable manifolds associated with the L_1 northern halo orbit, and blue denotes the stable manifold associated with the L_2 southern halo orbit. To search for a connection between the L_1 and L_2 orbits, locate points on the map that compare closely in both position and velocity. To view the velocity information for each point on the map, vectors representing the y and z components of the manifold velocity at the intersection are 'attached' to each crossing position in Fig. 6(b). Points that lie very near the Earth correspond to high speeds; for visual clarity, the map in Fig. 6(b) includes only those points that lie beyond 3 Earth radii. The red and blue contours, formed by the points on the map, intersect at two locations: one very near the Earth and one further away. A closer view of the intersection that lies further from the Earth reveals that the vectors at these locations are of similar

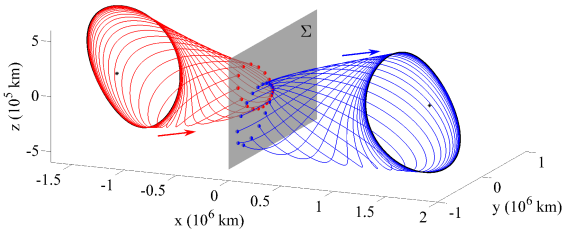

a) Planar projection

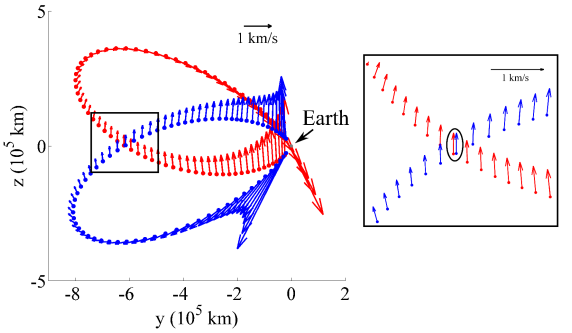

b) Planar projection

Fig. 6 Map associated with manifolds corresponding to northern L_1 and southern L_2 halo orbits for $C = 3.00074$; Earth-centered view

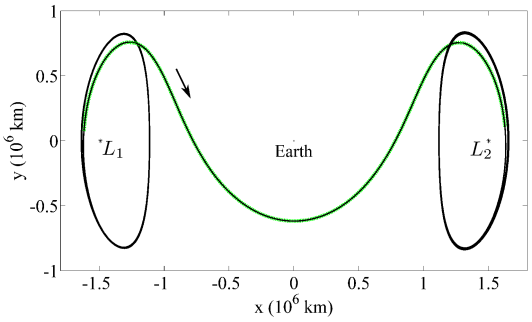

a) Planar projection

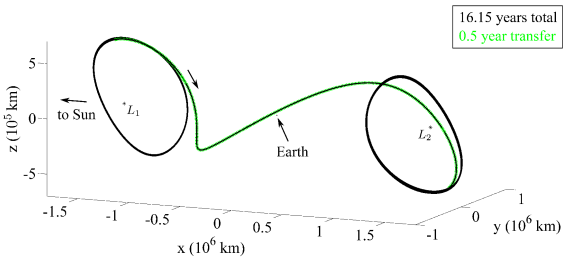

b) Spatial view

Fig. 7 Free transfer between northern L_1 and southern L_2 quasi-halo orbits, Earth-centered view

magnitude and orientation, indicating that $\dot{y}$ and $\dot{z}$ compare closely between the stable and unstable manifold crossings. Thus, a heteroclinic connection may exist nearby. To generate an initial guess for the heteroclinic connection, a stable and unstable manifold pair is selected from the map, and are circled in black in Fig. 6(b). The corrections algorithm, outlined previously, for heteroclinic connections between periodic orbits is employed, however the corrector chatters at $\|\bar{F}\| \sim 7 \times 10^{-4}$ (corresponding to errors on the order of $\sim 10^5$ km and ~ 10 m/s), suggesting that there may not exist a free transfer between periodic orbits in the vicinity of the initial guess. For this reason, the constraint that the halo orbits be precisely periodic is relaxed and a connection between quasi-periodic orbits is sought. To search for a connection, 15 revolutions along each halo orbit are incorporated into the initial guess and the targeting algorithm for connections between quasi-periodic orbits is employed. The resulting maneuver-free connection between L_1 and L_2 quasi-halo orbits, closely bound to the periodic orbits from the initial guess, appears in Fig. 7. By the symmetry properties of the CR3BP, a connection directed from the L_2 to the L_1 orbit is obtained through the transformation $y \to -y$, $\dot{x} \to -\dot{x}$, $\dot{z} \to -\dot{z}$.

Heteroclinic Connections between Northern and Southern Halo Family Members

In the following example, maps displaying invariant manifolds associated with halo orbits are demonstrated in the search for heteroclinic connections between members of the northern and southern halo orbit families associated with a single libration point, either L_1 or L_2. To compute such connections in the vicinity L_1, both the northern and southern L_1 halo orbits are computed for a Jacobi value of $C = C_{L_2} - 0.1 \approx 3.072$ (note that the southern orbit is simply obtained through the transformation $z \to -z$, $\dot{z} \to -\dot{z}$. The unstable manifold (red) associated with the northern halo orbit and the stable manifold (blue) generated from the southern halo are propagated until reaching an intersection with the one-sided surface of section defined by $x = 1 - \mu$, $\dot{x} > 0$; the resulting map appears in Fig. 8. From this map, initial guesses for two

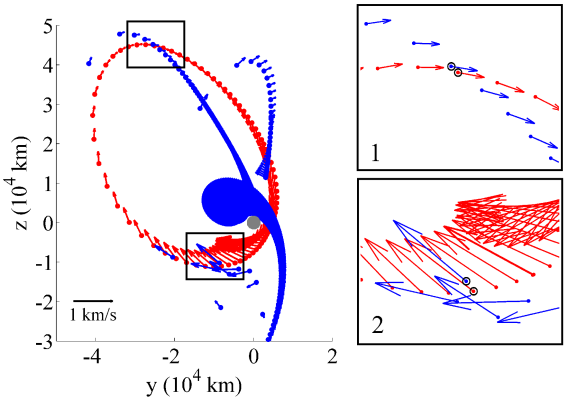

Fig. 8 Map associated with manifolds of northern and southern L_1 halo orbits for $C = C_{L_2} - 0.1$, Moon-centered view

potential heteroclinic connections are identified within the zoomed views numbered 1 and 2 in Fig. 8, where the base points corresponding to the manifolds that were initially selected to generate the initial guesses are circled in black. The previously defined corrections algorithm for heteroclinic connections between periodic

orbits is employed, and is successfully employed to locate the free transfers that appear in Figs. 9-10. The final Jacobi values for these arcs are $\sim C = 3.0723$ and $\sim C = 3.0768$, respectively. Continuity along the manifold arcs and periodic orbits is enforced with a tolerance of 1×10^{-12}, corresponding to $\sim 10^{-4}$ m in position and $\sim 10^{-12}$ m/s in velocity. The step size off the orbit and onto each manifold is $d = 20$ km; the initial/final manifold states along the unstable/stable manifolds are propagated in reverse-/forward-time (toward the halo orbits) for twice the orbit period; clearly, the manifolds remain in the vicinity of the halo orbits for at least two revolutions.

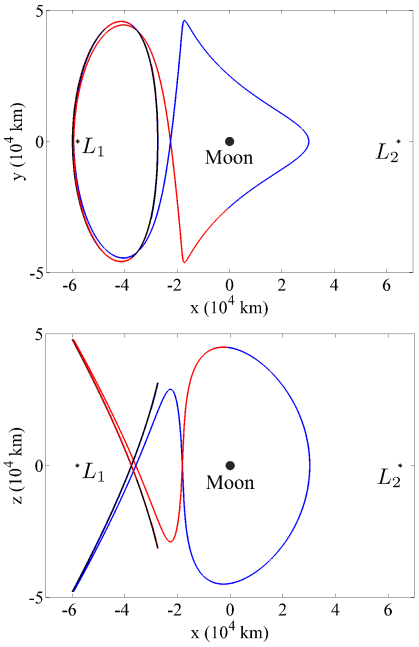

Fig. 9 Corrected heteroclinic connection between northern and southern L_1 halo orbits for initial guess 1, Moon-centered view; travel time along manifolds is 39.98 days

To search for heteroclinic connections between northern and southern L_2 halo orbits near the same level of Jacobi constant, $C = C_{L_2} - 0.1$, a map associated with the manifolds is generated. The map in Fig. 11 depicts positive crossings ($\dot{x} > 0$) of the $x = 1 - \mu$ surface for the unstable manifolds (red) departing from the northern L_2 halo and the stable manifolds (blue) associated with the southern halo orbit. A potential heteroclinic connection is identified (circled in the zoomed view in Fig. 11) and supplies the initial guess for the heteroclinic connection. Employing the differential corrections process, including periodicity constraints for the halo orbits, yields the heteroclinic connection plotted in Fig. 12. Again, the initial/final manifold states along the unstable/stable manifolds are propagated in reverse-/forward-time for twice the orbit period and remain in the vicinity of the periodic orbit.

Clear symmetries exist for the heteroclinic connections demonstrated in Figs. 9, 10 and 12, however, these transfers between northern and southern halos do not appear to exist throughout the entire halo family; perturbing the initial guess before applying the differential corrections process yields the precise heteroclinic connection located from the unperturbed initial guess (both converged solutions correspond to the same value of Jacobi constant), indicating that this type of heteroclinic connection likely does not exist for other halo orbits near the initial guess. Transfers from the southern to the northern halo orbits are obtained by reflecting the transfers in Figs. 9, 10, and 12 about the $x - y$ plane.

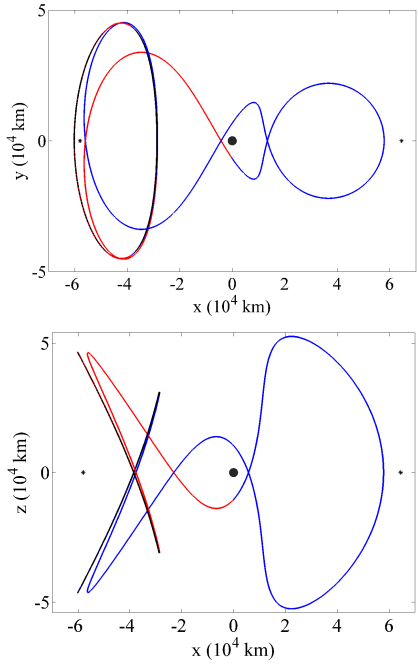

Fig. 10 Corrected heteroclinic connection between northern and southern L_1 halo orbits for initial guess 2, Moon-centered view; travel time along manifolds is 43.75 days

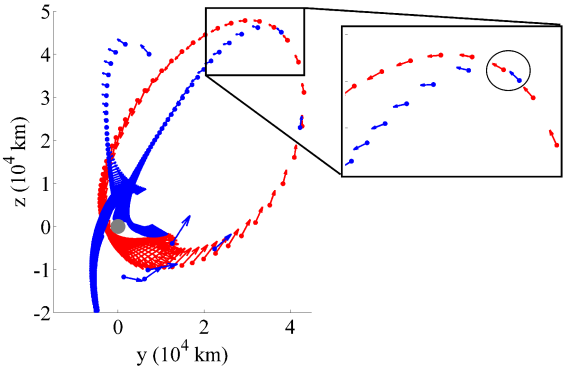

Fig. 11 Map associated with manifolds of northern and southern L_2 halo orbits corresponding to $C = C_{L_2} - 0.1$

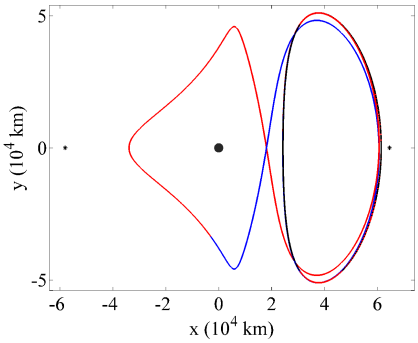

a) Planar projection

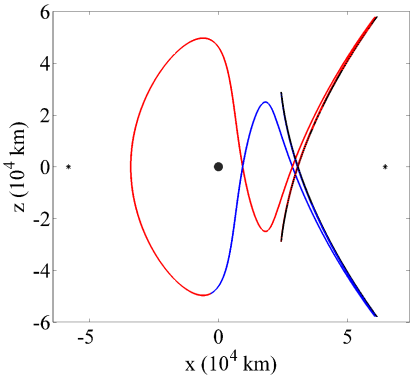

b) Spatial view

Fig. 12 Heteroclinic connection between northern and southern L_2 halo orbits, Moon-centered view; travel time along manifolds is 47.49 days

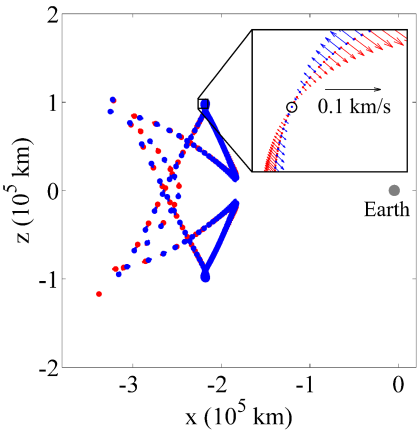

a) $C = 2.848$, $\dot{y} < 0$

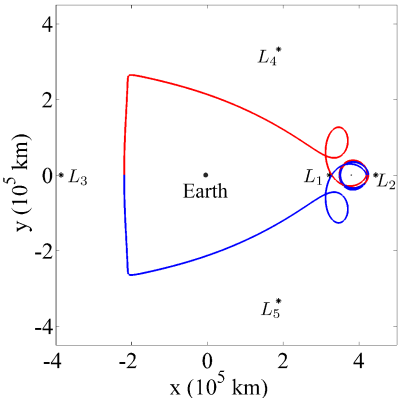

b) Planar Projection

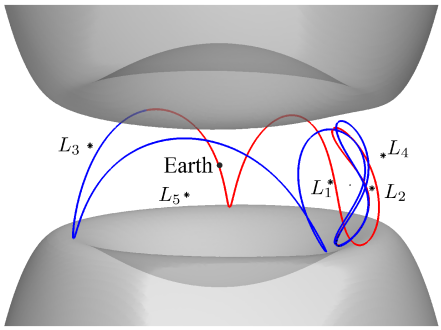

c) Spatial view

Fig. 13 Map of L_2 vertical orbit manifold crossings of the $y = 0$ surface for $C = 2.848$ and a homoclinic orbit located from the map in the Earth-Moon system; travel time along manifolds ~ 138 days

Homoclinic Connections associated with Vertical Orbits

The vertical orbit families, emanating from each of the libration points,[11] are composed of orbits that are symmetric across both the $x - y$ and $x - z$ planes, with many members that are highly inclined relative to P_1 and P_2. Higher-dimensional Poincaré map representations prove useful in the search for potential homoclinic connections associated with the vertical orbits, and are demonstrated for several energy levels in Figs. 13-16. One-sided maps, corresponding to the surface of section $\Sigma = \{y = 0\}$, appear for several values of Jacobi constant: manifolds propagated into the interior region are displayed on the maps in Figs. 13(a), 14(a), and 16(a), while manifolds propagated into the exterior region appear on the map in Fig. 15. In each example, an initial guess for the homoclinic connection is located and the corresponding manifold crossings are circled on the maps. The corrections algorithm to locate homoclinic connections associated with periodic orbits is employed and yields the transfers appearing in Figs. 13-16. The corrected trajectories are continuous to an order of 10^{-12}, corresponding to $\sim 10^{-4}$ m in position and $\sim 10^{-12}$ km/s in velocity. The step off of the periodic orbit and onto each manifold is $d = 20$ km; the initial/final manifold states along the unstable/stable manifolds are propagated in reverse-/forward-time for twice the orbit period, demonstrating that the manifolds remain in the vicinity of the periodic orbit for at least two revolutions in each example. Due to the symmetries that exist in the CR3BP, for each point on the maps in Figs. 13-16 there exists a counterpart that is reflected across the $x - y$ plane so that $z \rightarrow -z$ and $\dot{z} \rightarrow -\dot{z}$. Thus, for each homoclinic connection depictedn there exists a second connection computed by reflecting these trajectories across the $x - y$ plane.

Homoclinic connections associated with libration point orbits in the Sun-Earth system offer a means for

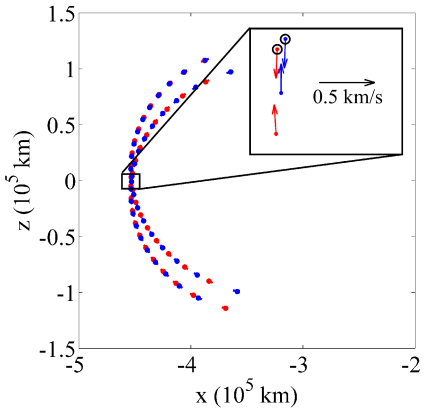

a) $C = 2.8$, $\dot{y} > 0$

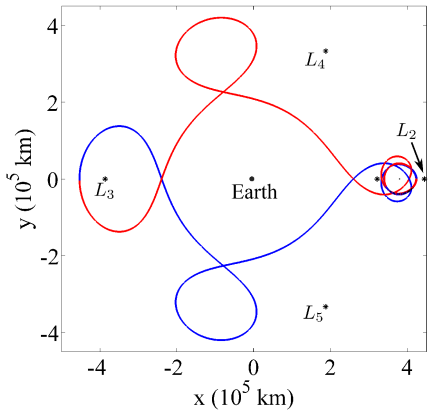

b) Planar Projection

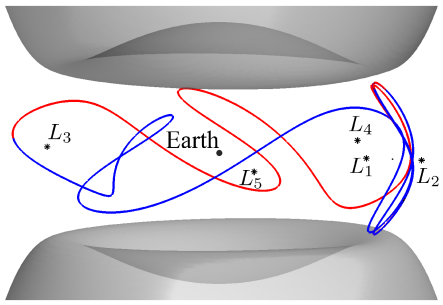

c) Spatial view

Fig. 14 Map of L_2 vertical orbit manifold crossings of the $y = 0$ surface for $C = 2.8$ and a homoclinic orbit located from the map in the Earth-Moon system; travel time along manifolds ~ 142 days

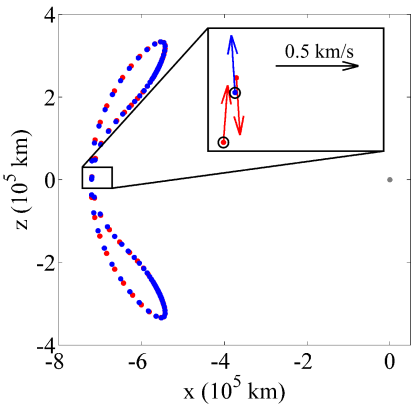

a) $C = 2.7$, $\dot{y} > 0$

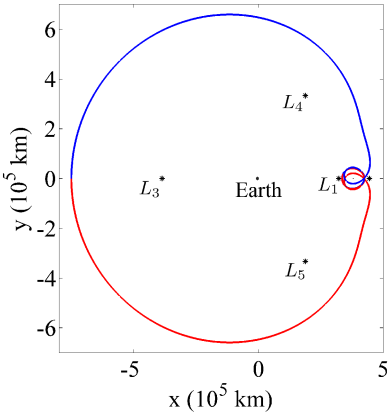

b) Planar Projection

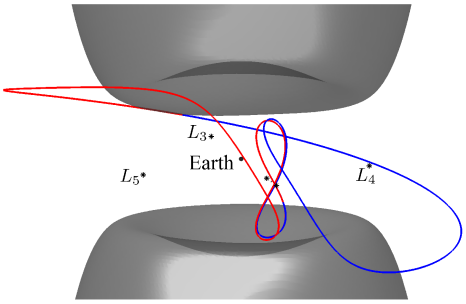

c) Spatial view

Fig. 15 Map of L_2 vertical orbit manifold crossings of the $y = 0$ surface for $C = 2.7$ and a homoclinic orbit located from the map in the Earth-Moon system; travel time along manifolds ~ 119 days

transport around the Earth's orbit, with many arcs passing by the L_4 and L_5 libration points. To locate a homoclinic transfer in the Sun-Earth system, a map of the stable/unstable manifold crossings associated with a vertical orbit for an energy level between the values of C for the L_2 and L_3 points appears in Fig. 17. Selecting the manifolds circled within the zoom view in Fig. 17(a) to supply the initial guess for the homoclinic connection, a continuous transfer is located using the differential corrections algorithm, including periodicity constraints for the vertical orbits, and is displayed in Figs. 17(b)-17(c). Because of the large in-plane amplitudes in the Sun-Earth system, the out-of-plane amplitudes are obscured, although the manifolds in this connection oscillate between $\sim \pm 2.28 \times 10^6$ km with a period of about 1 year. To achieve a transfer with larger z-amplitudes, a higher energy level, i.e., a *lower* value of Jacobi constant, is considered. The map in Fig. 18(a) represents intersections of the stable/unstable manifolds associated with an L_1 vertical orbit for $C = 0.95 \cdot C_{L_4} \approx 2.85$; note that the z-amplitudes have increased by more than an order of magnitude compared with the manifold crossings in Fig. 17(a). A pair of stable/unstable manifolds is

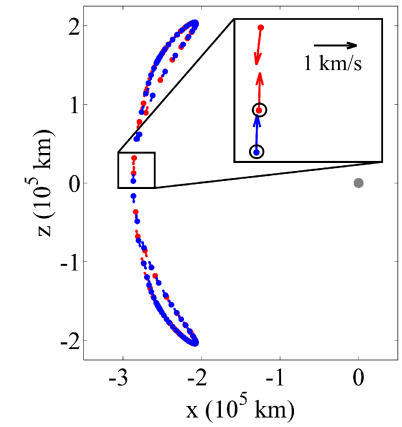

a) $C = 2.5$, $\dot{y} < 0$

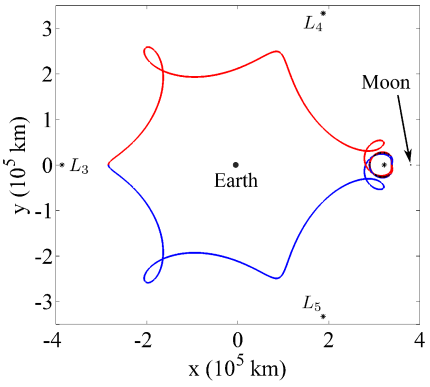

b) Planar Projection

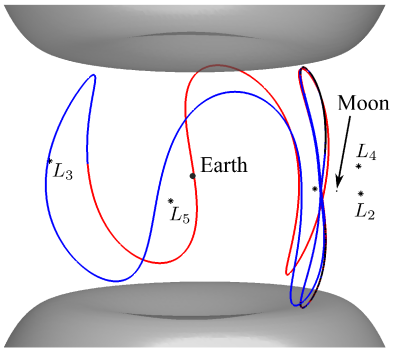

c) Spatial view

Fig. 16 Map of L_1 vertical orbit manifold crossings of the $y = 0$ surface for $C = 2.5$ and a homoclinic orbit located from the map in the Earth-Moon system; travel time along manifolds ~ 125 days

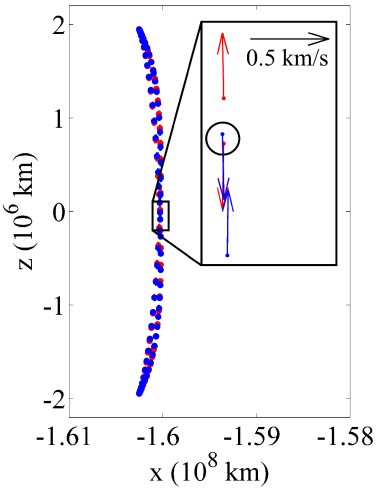

a) $C = 3.0005375$, $\dot{y} > 0$

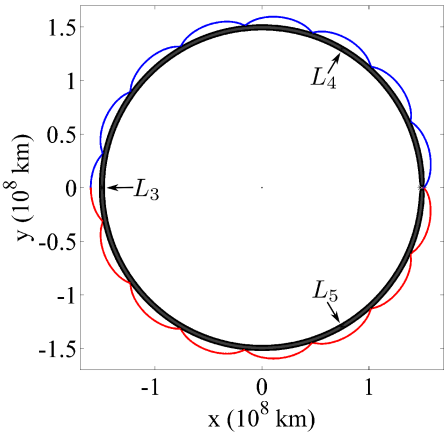

b) Planar projection

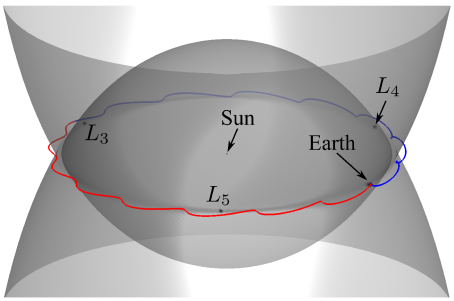

c) Spatial view

Fig. 17 Map of L_2 vertical orbit manifold crossings of $y = 0$ surface for $C = 3.0005375$ and a homoclinic orbit located from the map in the Sun-Earth system; travel time along manifolds is 17.27 years

identified that nearly overlap on the Poincaré map in Fig. 18(a), and is circled in black; these manifolds represent the initial guess for a homoclinic connection. Application of the differential corrections algorithm including a constraint on the periodicity of the vertical orbits leads to divergent behavior, however. Thus, the periodicity constraint is relaxed and 5 revolutions along the vertical orbits are incorporated into the initial guess to search for a connection between quasi-periodic orbits in the vicinity of the vertical orbit. The resulting maneuver-free connection between quasi-periodic orbits (tightly bound to the vertical orbits that are defined as the initial guess) appears in Fig. 18. The orbit of the Sun-Earth Trojan asteroid 2010 TK_7 from October 1, 2012 to October 1, 2050 is also plotted in Fig. 18 (in green) to provide a reference for the z-amplitude of the vertical orbit and the associated transfer. The time-of-flight associated with the asteroid path is roughly equal to the time required to travel along the segment of the transfer path that

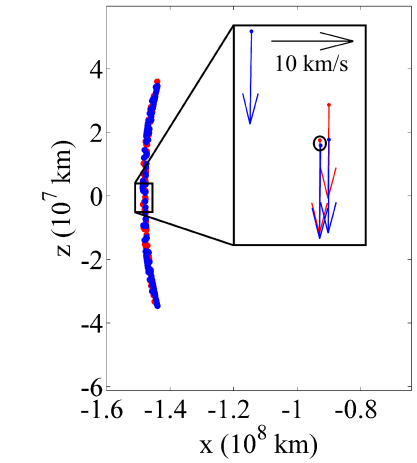

a) $C = 2.85$, $\dot{y} > 0$

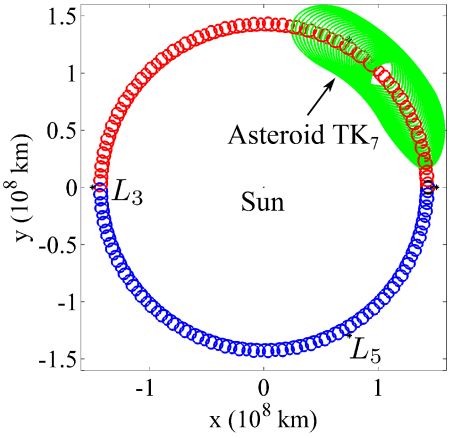

b) Planar projection

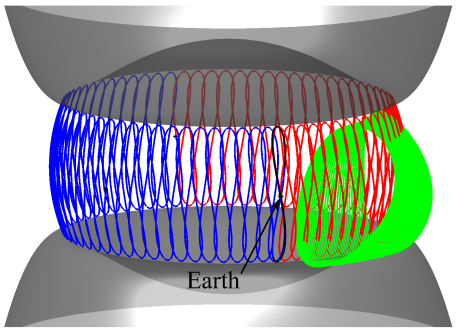

c) Spatial view

Fig. 18 Map of L_1 vertical orbit manifold crossings of $y = 0$ surface for $C = 2.85$ and a maneuver-free transfer located from the map in the Sun-Earth system; travel time along manifolds is 75.00 years

is plotted in red.

Periapse Maps in the Spatial Problem

The periapse surface of section, initially demonstrated by Paskowitz,[25] Scheeres,[25,31] and Villac,[31] is useful as one of a number of tools for the characterization of trajectories in the CR3BP. The periapse map is defined by the surface of section $\Sigma = \{\dot{\rho} = 0\}$, where ρ is the radius between the satellite and the primary body. Periapsis and apoapsis are distinguished by the radial acceleration, i.e., $\ddot{\rho} > 0$ at periapsis and $\ddot{\rho} < 0$ at apoapsis. Periapse maps have been employed by several researchers[6,7,14,16] to demonstrate their use in various mission design scenarios.

Consider the planar periapse map corresponding to $C = 3.15$ in the Earth-Moon system, plotted in Fig. 19. To generate this map, a grid of prograde apses is defined over the region within the zero-velocity curves (ZVCs) and for values of x such that $x_{L_1} \leq x \leq x_{L_2}$, i.e., initial conditions for which $\dot{\rho} = 0$. These initial conditions are propagated for 2.5 years in both forward- and reverse-time and the following events are recorded: (i) each passage of periapsis; (ii) escape through the L_1 gateway as marked by crossing $x = x_{L_1} - 0.1$; (iii)escape through the L_2 gateway by crossing $x = x_{L_2} + 0.1$, where 0.1 is a nondimensional distance. Trajectories that cross either of the boundaries $x = x_{L_1} - 0.1$ or $x = x_{L_2} + 0.1$ are termed transit trajectories; those that do not cross either boundary are designated as non-transit trajectories, or long-term captures (note that these long-term 'capture' orbits may still escape the vicinity of the Moon beyond the 5-year interval). All periapses along L_1 and L_2 transits are plotted in Fig. 19 in gray, and periapses along non-transit trajectories appear in green (only prograde periapses appear in the figure). For this energy level, the vast majority of the planar trajectories escape from the vicinity of the Moon; most of the long-term captures that appear on the map impact the Moon. As previously demonstrated by Conley,[5] Koon et al.,[19] and Gómez et al.,[12] among others, planar transit trajectories are trajectories that lie within the manifold tubes associated with the L_1 and L_2 Lyapunov orbits for a given energy level; Paskowitz,[25] Scheeres,[25,31] and Villac[31] use periapse maps to classify transit trajectory behavior. To highlight the relationship between transit

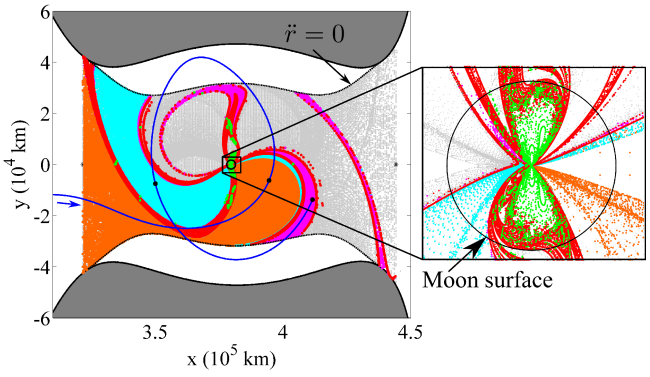

Fig. 19 Planar periapse map depicting periapses along transit (gray, orange, cyan, magenta) and non-transit (green) trajectories for $C = 3.15$ in the Earth-Moon system; a sample L_1 transit (blue) is also plotted

trajectories and planar Lyapunov manifolds, periapses along L_1 Lyapunov unstable manifolds are plotted in red in Fig. 19, and the first three periapses, along L_1

transits, after entry through the L_1 gateway appear in orange, cyan, and magenta, respectively. The contours formed by manifold periapses bound the colored regions formed by transit periapse passages. A sample transit, plotted in blue in Fig. 19, is computed by selecting a periapsis within the magenta L_1 transit region and propagating in reverse-time. The contour, $\ddot{\rho} = 0$, delineating regions of periapsis and apoapsis for prograde apses is represented by a dotted black line.

For periapse maps in the spatial problem, the map cannot be fully represented using four Cartesian state space variables and the four-dimensional map is rendered in spherical coordinates. This representation may not be intuitive, but to transform the map to Cartesian coordinates requires that the map represent all six states, as demonstrated in Fig. 4(b). To produce a periapse map in the spatial problem, a grid of positions within the zero-velocity surface (ZVS) and bordered by $x_{L_1} \leq x \leq x_{L_2}$ is generated; for each position location, a range of velocities are assigned such that $C = 3.15$, $\dot{\rho} = 0$ and each apse is prograde. To exploit the symmetries of the CR3BP, only points for which $z \geq 0$ are included in the grid of initial conditions; reflecting the trajectories, obtained by integrating the initial conditions from the grid, across the $x-y$ plane reveals the orbits that are generated by propagating initial conditions for which $z < 0$. These

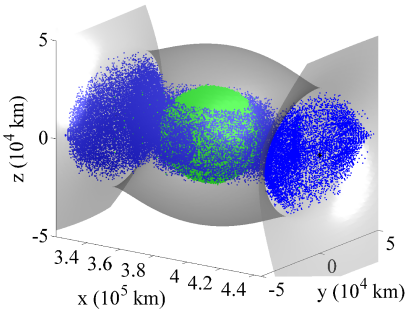

Fig. 20 Periapse map, projected into configuration space, depicting periapses along transit (blue) and non-transit (green) trajectories for $C = 3.15$ in the Earth-Moon system

initial conditions are propagated for 2.5 years in the Earth-Moon system in both forward- and reverse-time; each passage of periapsis, escape through the L_1 gateway, and escape through the L_2 gateway are again recorded for each integration. A projection of the periapse map associated with the resulting transit (blue) and non-transit (green) trajectories for $C = 3.15$ appears in Fig. 20.

A large variety of long-term capture trajectories exist in the SCR3BP, including periodic orbits. Because the crossings of the periapse map belong to trajectories generated from randomly selected initial conditions, it is unlikely that a periodic orbit will appear directly on the map; however, stable periodic orbits may be located by observing the behavior of nearby crossings on the map. For example, consider the map in Fig. 21(a); this map represents a zoomed view of periapses corresponding to long-term capture trajectories on the left of the Moon in Fig. 20, now plotted using chains that represent all six Cartesian state variables associated with each periapsis, as demonstrated in Fig. 4(b). The solid points represent the x, y location of the periapses, and each chain is colored according to inclination relative to the Moon (low/high inclinations correspond to blue/red). A group of four cyan chains (including one circled in red) surround a central chain that is circled in green; these four chains are labelled 1-4 on the map. From visual inspection of the location and geometry of the chains, it is evident that each of these four periapses possesses values of y, $\dot{x}$ and $\dot{z}$ that are nearly zero. It is also apparent that $z < 0$ for periapses 1 and 3, whereas $z > 0$ for periapses 2 and 4. These periapses are in a mirror configuration,[28] that is, P_3 lies in the same plane as P_1 and P_2, and the velocity vector defined for P_3 is normal to that plane. If this configuration occurs twice, then the orbit is periodic. A similar structure appears to the right of the Moon, as demonstrated in Fig. 21(b) where a number of green and blue colored periapses occur near $y = 0$ with apparently small $\dot{x}$ and $\dot{z}$ magnitudes. To seed an

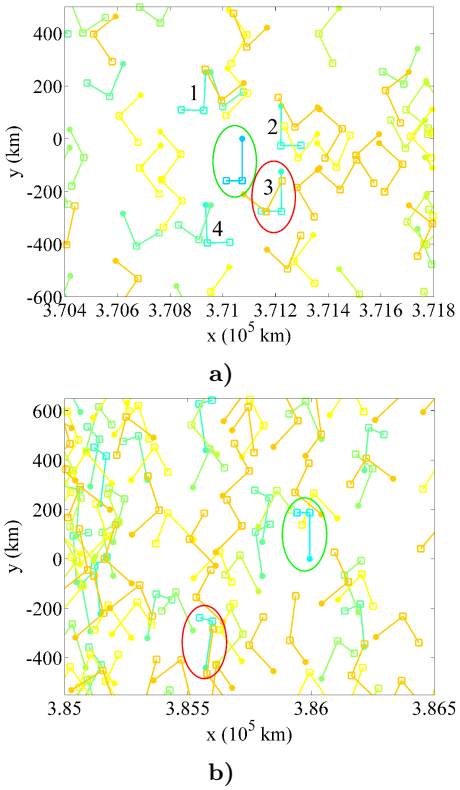

Fig. 21 Poincaré maps representing periapses along non-transit trajectories for inclinations $0° \leq i \leq 70°$ in the Earth-Moon system

initial guess for a periodic orbit in the vicinity of the periapses in these maps, the periapses circled in red in Figs. 21(a), 21(b) are employed. As an example,

consider the red circled periapsis in Fig. 21(b). This periapsis, for which $z < 0$, is propagated in reverse-time until it again intersects the surface defined by $y = 0$, $\dot{y} > 0$, yielding the red arc that appears in Fig. 22(a). The open red circle represents the location of the periapsis selected from the map in Fig. 21(b). For a periodic orbit, a second mirror configuration is expected at $y = 0$, $z > 0$; thus, the red arc is reflected across the $x - y$ plane, yielding the green arc. The initial guess for the periodic orbit is composed of the red arc, which is re-integrated in forward-time, concatenated with the green arc, also integrated in forward-time. To aid convergence, the red and green arcs are sampled, as depicted in Fig. 22(a), and integrated in segments. To enforce periodicity of the orbit, a differential corrections process is employed in which the quantities contained in $\bar{X}_p$ are allowed to vary to satisfy the constraint $\bar{F}_p = \bar{0}$:

$$\bar{X}_p = \begin{bmatrix} \bar{x}_1(t_{10}) \\ \bar{x}_2(t_{20}) \\ \vdots \\ \bar{x}_n(t_{n0}) \\ t_{1f} \\ t_{2f} \\ \vdots \\ t_{nf} \\ \beta \end{bmatrix}, \quad \bar{F}_p = \begin{bmatrix} \bar{x}_2(t_{20}) - \bar{x}_1(t_{1f}) \\ \vdots \\ \bar{x}_n(t_{n0}) - \bar{x}_{n-1}(t_{n-1f}) \\ x_n(t_{nf}) - x_1(t_{10}) \\ y_n(t_{nf}) - y_1(t_{10}) \\ z_n(t_{nf}) - z_1(t_{10}) \\ \dot{x}_n(t_{nf}) - \dot{x}_1(t_{10}) \\ \dot{y}_n(t_{nf}) - \text{sign}(\dot{y}_1(t_{10})) \cdot \beta^2 \\ \dot{z}_n(t_{nf}) - \dot{z}_1(t_{10}) \end{bmatrix}$$

This corrections process yields the periodic orbit plotted in black in Fig. 22(a), as well as in red (thin line) in Fig. 22(b) with the eccentricity oscillating between 0.1 and 0.7, and inclincation oscillating between 37° and 43° (orbits of this geometry are demonstrated by Lara and Russel[20]). This same process is employed to locate a periodic orbit corresponding to an initial guess generated from periapsis 3, circled in red in Fig. 21(a), yielding the bold red orbit in Fig. 22(b) with the eccentricity oscillating between 0.2 and 0.65, and inclincation oscillating between about 33° and 37°. The periapses for which $z < 0$ along these periodic orbits are plotted within the green circles on the maps in Fig. 21. While the orbits in Fig. 22 are unstable, the maximum real part of the eigenvalues associated with each monodromy matrix is very small, (approximately 5 and 3, respectively), indicating that the orbits are nearly stable. Employing a pseudo-arclength continuation scheme, initialized from the orbits in Fig. 22(b), families of lunar orbits are computed; sample family members are displayed in Fig. 23, where stable and unstable orbits are colored blue and red, respectively.

In addition to the computation of long-term capture orbits about the Moon, periapse maps are also useful to locate transfers to such orbits. Consider the transit trajectories corresponding to the blue periapses in Fig. 20; the first periapses along the subset of these trajectories that enter through the L_1 gateway, i.e., the first periapses after entry through the L_1 gateway along L_1 transit trajectories, are displayed in Fig. 24(a). The full states associated with these periapses are represented using glyphs, where the solid points locate the x, y point at periapsis, and the glyphs are vector chains defined as in Fig. 4(b); each periapsis is colored by inclination relative to the $x - y$ plane where low/high inclinations correspond to blue/red. A close view of the black box in Fig. 24(a) appears in Fig. 24(b), in addition to the $z < 0$ periapsis, circled in green, from the black periodic orbit in Fig. 22(a). A transit periapsis, basepoint circled in black, is identified through visual inspection of the map, that is, nearby the periodic orbit periapsis location and with a similar velocity state. Integrating this periapse state in reverse-time yields an L_1 transit trajectory that serves as an initial guess for a transfer onto the periodic orbit from the vicinity of the Earth. A discontinuity of ~ 700 km and ~ 70 m/s exists between the transit periapsis and the periapsis along the periodic orbit. This discontinuity is removed using a differential corrections process to enforce continuity in position, and to restrict the velocity discontinuity to a maximum value of 5 m/s (note that this sample transfer is not optimized). The resulting transit trajectory is plotted in blue in Fig. 25. A transfer from a 200 km altitude circular Earth orbit to the transit apoapsis, relative to Earth, is included in green. The total ΔV required is approximately 3.74 km/s (633 m/s to insert onto the

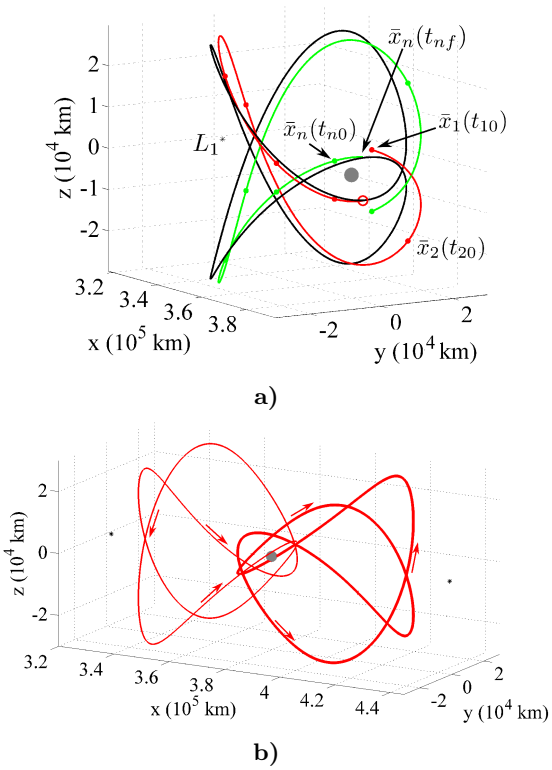

Fig. 22 Two periodic orbits computed using initial guesses from maps in the Earth-Moon system

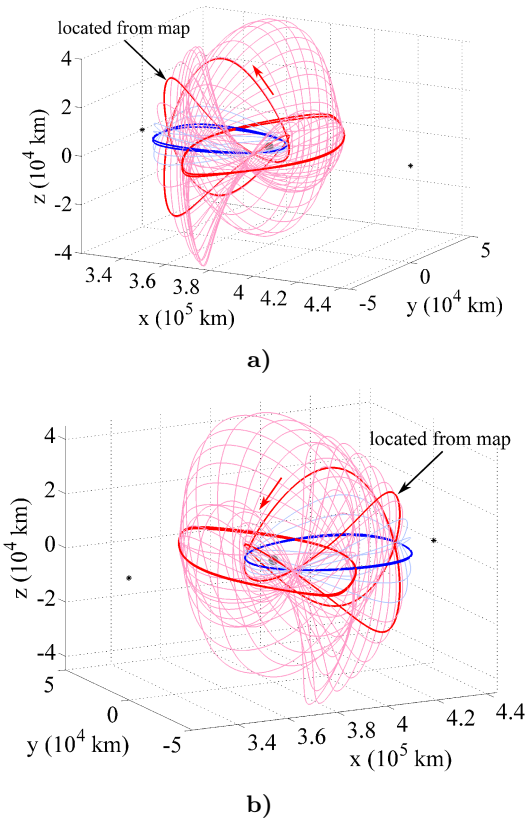

Fig. 23 Families of periodic orbits initialized from Poincaré maps in the Earth-Moon system

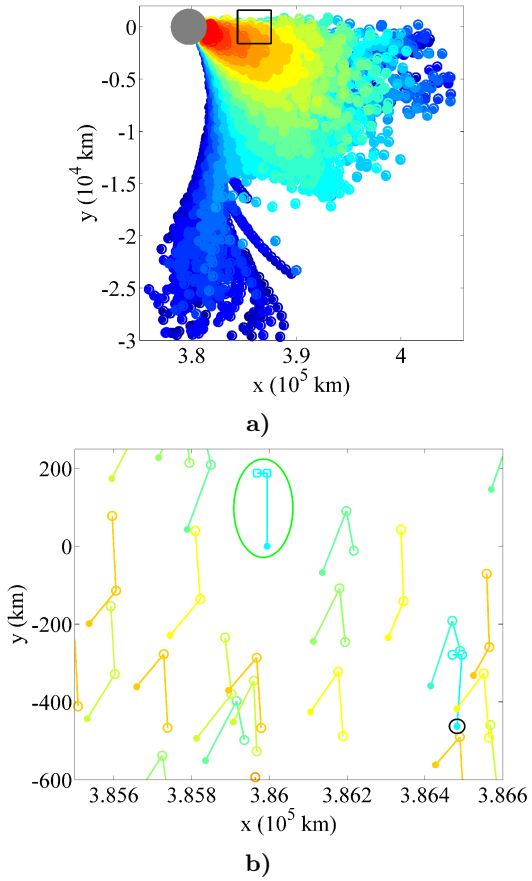

Fig. 24 Periapse map employed to locate a transfer between Earth and a periodic orbit near the Moon

transit path and 5 m/s to transfer onto the periodic orbit). The combined time-of-flight along the green and blue transfer trajectories is 21.08 days, and the black periodic orbit has a period of roughly 14 days.

Conclusions

The Circular Restricted Three-Body Problem (CR3BP) serves as a useful framework for preliminary trajectory design in a multi-body force environment, however mission design in this dynamical regime is nontrivial. To facilitate trajectory design in such an environment, it is desirable to develop tools that provide insight into the available solution space. The Poincaré map is a powerful tool that has proven useful to evaluate the available solution space and to compute trajectories with specified characteristics. In combination with a constraint on energy level, Poincaré maps allow a reduction in dimension such that, for the planar problem, the system is reduced to two-dimensions and the phase space is fully represented by the projection onto a plane. In the spatial problem, however, Poincaré maps must represent at least four states and are therefore challenging to visualize.

In this investigation, a method to represent the information in higher-dimensional Poincaré maps using a planar visualization is explored and is applied to trajectory design. Four-dimensional map representations are demonstrated to display the invariant manifolds associated with both halo and vertical orbits in the spatial problem for the Earth-Moon and Sun-Earth systems. Through visual inspection of these maps, free transfers (heteroclinic and homoclinic connections) associated with a variety of periodic and quasi-periodic orbits are located. Alternative maps, such as the periapse Poincaré map, require that all of the six Cartesian states be represented. Sample six-dimensional periapse map representations are generated. Visual examination of the maps reveals structures that suggest the existence of nearby periodic orbits. An initial guess, computed from the map, is generated to facilitate a differential corrections process to locate these orbits. Two symmetric lunar orbits are located and are provide a starting point to generate families of periodic orbits about the Moon via numerical continuation. The higher-dimensional periapse map representations are additionally employed to locate transfers to these orbits via transit trajectories.

Acknowledgments

The authors wish to thank the Purdue University Graduate School, the College of Engineering, and the School of Aeronautics and Astronautics for providing funding in support of this work. Additional support through a Purdue Doctoral Fellowship is also appreci-

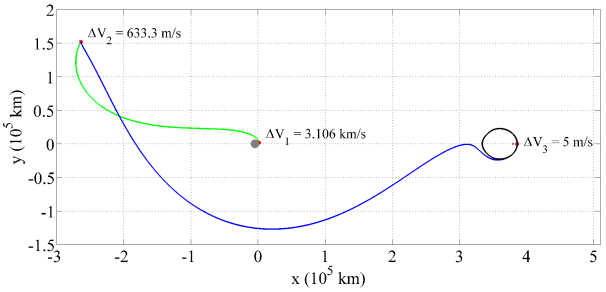

a) Planar projection

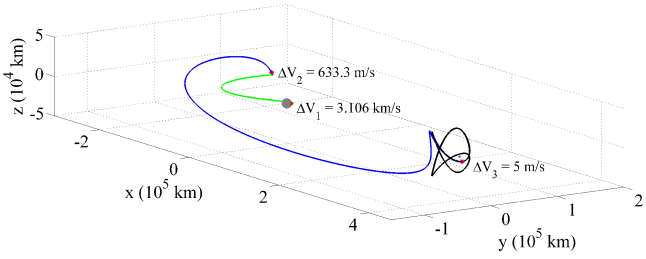

b) Spatial view

Fig. 25 Transfer from 200 km LEO to large lunar orbit

ated. Many thanks to Ph.D. student Wayne Schlei for his suggestions and insight.

References

[1]Barrabés, E., Mondelo, J. M., Ollé, M.: Numerical continuation of families of homoclinic connections of periodic orbits in the RTBP. Nonlinearity 22, 2901-2918 (2009)

[2]Barrabés, E., Mondelo, J. M., Ollé, M.: Dynamical aspects of multi-round horseshoe-shaped homoclinic orbits in the RTBP. Celest. Mech. Dyn. Astr. 105, 197-210 (2009)

[3]Bray, T. A., Goudas, C. L.: Doubly Symmetric Orbits about the Collinear Lagrangian Points. Astron. J. 72, 202-213 (1967)

[4]Breakwell, J. V., Brown, J. V.: The 'halo' family of 3-dimensional periodic orbits in the earth-moon restricted 3-body problem. Celest. Mech. 20, 389-404 (1979)

[5]Conley, C. C.: Low energy transit orbits in the restricted three-body problem. Soc. for Ind. and Appl. Math. J. on Appl. Math. 16, 732-746 (1968)

[6]Davis, D. C., Howell, K. C.: Trajectory evolution in the multi-body problem with applications in the Saturnian system. Acta Astron. 69, 1038-1049 (2011)

[7]Davis, D. C., Howell, K. C.: Characterization of trajectories near the smaller primary in the restricted problem for applications. J. of Guid., Control, and Dyn. 35, 116-128 (2012)

[8]Dichmann, D., Doedel, E., Paffenroth. R.: The Computation of Periodic Solutions of the 3-Body Problem Using the Numerical Continuation Sofware AUTO. In: Gómez, G., Lo, M., Masdemont, J. (eds.) Libration Point Orbits and Applications, pp. 489-528. The University of Arizona Press, Tucson (2003)

[9]ESA, Herschel and Planck Overview, [Accessed September 7, 2012]. http://www.esa.int/esaMI/herschelplanck/index.html.

[10]Farquhar, R. W., Kamel, A. A.: Quasi-periodic orbits about the translunar libration point. Celest. Mech. 7, 458-473 (1973)

[11]Grebow, D.: Generating Periodic Orbits in the Circular Restricted Three-Body Problem with Applications to Lunar South Pole Coverage. M.S. Thesis, School of Aeronautics and Astronautics, Purdue University, West Lafayette, Indiana (2006)

[12]Gómez, G., Koon, W. S., Lo, M. W., Marsden, J. E.: Connecting orbits and invariant manifolds in the spatial restricted three-body problem. Nonlinearity 17, 1571-1606 (2004)

[13]Gómez, G., Marcote, M., Mondelo, J. M.: The invariant manifold structure of the spatial Hills problem. Dyn. Syst.: An Int. J. 20, 115-147 (2005)

[14]Haapala, A. and Howell, K.: Trajectory design using periapse Poincaré maps and invariant manifolds. 21st AAS/AIAA Space Flight Mechanics Meeting, New Orleans, Louisiana, February (2011)

[15]Howell, K. C.: Families of orbits in the vicinity of the collinear libration points. J. of the Astron. Sci. 49, 107-125 (2001)

[16]Howell, K. C., Davis, D. C., Haapala, A. F.: Application of periapse maps for the design of trajectories near the smaller primary in multi-body regimes. J. of Math. Probl. in Eng., Special Topic: Mathematical Methods Applied to the Celestial Mechanics of Artificial Satellites 2012, 1-22 (2012). Article ID 351759

[17]Jorba, Á., Masdemont, J.: Dynamics in the center manifold of the collinear points of the restricted three body problem, Physica D 132, 189-213 (1999)

[18]Kolemen, E., Kasdin, J., Gurfil, P.: Quasi-periodic orbits of the restricted three-body problem made easy, New Trends in Astrodynamics and Applications III, AIP Conference Proceedings 886, 68-77, Princeton, New Jersey, August 16-18 (2007)

[19]Koon, W. S., Lo, M. W., Marsden, J. E., Ross, S. D.: Heteroclinic connections between periodic orbits and resonance transitions in celestial mechanics. Chaos 10, 427-469 (2000)

[20]Lara, M., Russell, R.P.: On the family 'g' of the restricted three-body problem. IX Jornadas de Trabajo en Mecanica Celeste, Jaca, Huesca, Spain, Jun 2006.

[21]NASA, ISEE-3 Overview, [Accessed September 7, 2012]. http://heasarc.gsfc.nasa.gov/docs/heasarc/missions/isee3.html.

[22]NASA, Missions, [Accessed September 7, 2012]. http://www.nasa.gov/missions/index.html.

[23]NASA, SOHO Overview, [Accessed September 7, 2012]. http://soho.nascom.nasa.gov/about/about.html.

[24]NASA, WMAP Mission, [Accessed September 7, 2012]. http://map.gsfc.nasa.gov/mission/.

[25]Paskowitz, M. E., Scheeres, D. J.: Robust capture and transfer trajectories for planetary satellite orbiters. J. of Guid., Control, and Dyn. 29, 342-353 (2006)

[26]Parker, J. S., Davis, K. E., Born, G. H.: Chaining periodic three-body orbits in the EarthMoon system. Acta Astron. 67, 623-638 (2010)

[27]Pickett, R., Grinstein, G.: Iconographic displays for visualizing multidimensional data. Proceedings IEEE Conference on Systems, Man, and Cybernetics 1, 514-519 (1988)

[28]Roy, A. E.: Orbital Motion. Institute of Physics, Bristol, United Kingdom (2005)

[29]Stuart, J., Ozimek, M., Howell, K. C.: Optimal, low-thrust, path-constrained transfers between libration point orbits using invariant manifolds. AIAA/AAS Astrodynamics Specialist Conference, Toronto, Canada, August (2010)

[30]Szebehely, V.: Theory of Orbits: The Restricted Problem of Three Bodies. Academic Press, New York, United States (1967)

[31]Villac, B. F., Scheeres, D. J.: Escaping trajectories in the Hill three-body problem and applications. J. of Guid., Control, and Dyn. 26, 224-232 (2003)

[32]Ward, M. O.: A taxonomy of glyph placement strategies for multidimensional data visualization. Inf. Vis. 1, 194-210 (2002)